

# Measurement and Modelling of Scattering From Buildings

Vittorio Degli-Esposti, *Member, IEEE*, Franco Fuschini, Enrico M. Vitucci, *Student Member, IEEE*, and Gabriele Falciasacca

**Abstract**—The results of a measurement campaign aimed at determining the far-field diffuse scattering pattern of typical building walls are shown in the paper. Such results are then used to determine and tune simple diffuse scattering models based on the effective roughness approach, to be embedded into ray tracing simulators. It is shown that by adopting an appropriate single-lobe scattering pattern the agreement between simulation and measurement is very good.

**Index Terms**—Radio propagation measurements, ray tracing, scattering.

## I. INTRODUCTION

RECENTLY, the adoption of ray tracing (RT) tools has greatly improved field prediction capabilities in urban environment and good results have been obtained in a variety of cases [1]–[4]. However, since conventional RT only accounts for rays that undergo specular reflections or diffractions, it fails to properly describe diffuse scattering phenomena which can have a significant impact on radio propagation in urban areas. As intended here, diffuse scattering refers to the signals scattered in other than the specular direction as a result of deviations (surface or volume irregularities) in a building wall from a uniform flat layer. Recent experimental studies have shown that diffuse scattering contributions due to buildings or even lampposts plays an important role in determining time and angle dispersion of radio signals in real environments [5]–[7]. The modeling of diffuse scattering from buildings is quite a difficult problem, since building wall irregularities cannot be modeled as Gaussian surface roughness, as assumed in most theoretical models. Few publications explicitly deal with modeling of diffuse scattering from buildings [8]–[12]. In particular, in [11] and [12] a simple “effective roughness” (ER) model for diffuse scattering from building walls has been proposed, and in [13] the same model has been inserted into a 3-D ray tracing program, showing a sensible improvement in the accuracy of wideband predictions versus measurements with respect to conventional RT. The ER model described in [11], [12], however, assumes that the wave impinging on a wall element (or on an entire wall if the wall is far from the radio

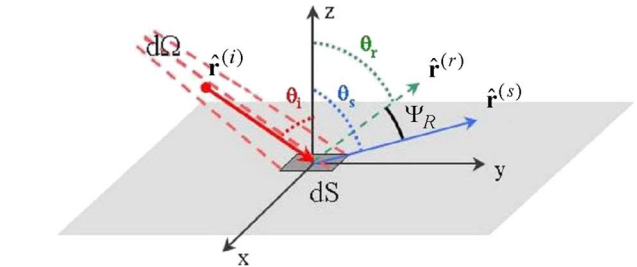


Fig. 1. A generic surface element producing reflection and diffuse scattering.

terminals) is scattered according to a Lambertian scattering pattern regardless of the direction of incidence.

In the present work the ER model has been modified by orienting the scattering pattern lobe toward the specular direction, which is more realistic, and re-shaping it in a number of different ways while preserving the physical consistency of the model (Section II). Then, the scattering pattern of real building walls has been measured using directive antennas and an appropriate measurement set-up (Section III).

Finally, the experimental scattering patterns have been compared with simulation obtained through the modified ER model embedded into a 3-D RT tool (Sections IV and V), thus determining the best scattering pattern shape and the best values of the scattering coefficient  $S$  in the considered cases. Results and conclusions are drawn in Sections VI and VII, respectively.

## II. THE DIFFUSE SCATTERING MODELS

The contribution of diffuse scattering to propagation is evaluated adopting the ER approach presented in [11], [12]. A sort of effective roughness is associated with each wall, which not only takes into account real surface roughness but also the wall irregularity effect in a mean, statistical way. In the ER model the field scattered by the generic wall element  $dS$  (Fig. 1) is modeled as a non uniform spherical wave which departs from the element and propagates in the upper half space. Precisely, the power density carried by the scattered wave is proportional to  $|\bar{E}_s|^2 = |\bar{E}_s(r_s, \theta_s, \phi_s)|^2$ , where  $\bar{E}_s$  is the intensity of the scattered field, which is evaluated according to a proper scattering coefficient ( $S$ ) and a “scattering pattern,” both depending on the characteristics of wall irregularities (see below).

In order to account for a wide range of possible situations, different choices can be done in defining both the scattering coefficient and the scattering pattern, so different categories of models can be hypothesized.

We can distinguish between two different approaches.

Manuscript received December 29, 2005; revised July 7, 2006. This work was supported in part by the European Network of Excellence NEWCOM.

The authors are with the Università di Bologna-Dipartimento di Elettronica, Informatica e Sistemistica, 40136 Bologna, Italy (e-mail: vdegliespsti@deis.unibo.it; ffuschini@deis.unibo.it; evitucci@deis.unibo.it; gfalciasacca@deis.unibo.it).

Color versions of one or more of the figures in this paper are available online at <http://ieeexplore.ieee.org>.

Digital Object Identifier 10.1109/TAP.2006.888422

In the first approach the scattering parameter is defined as

$$S = \frac{|\overline{E}_S|}{|\overline{E}_i|} \Big|_{ds} \quad (1)$$

where  $|\overline{E}_i|$  and  $|\overline{E}_S|$  are the norms of the incident and scattered fields on the surface element  $ds$ , respectively. Since  $ds$  is infinitesimal, the fields are assumed constant on it. In other words,  $S^2$  is the percentage of the power impinging on the wall element which is spread in all directions. Following this approach, the overall power balance on the surface element  $ds$  can be written as [11], [12]:

$$1 = \Gamma^2 R^2 + S^2 + P_p/P_i \quad (2)$$

where  $\Gamma = |\overline{E}_R|/|\overline{E}_i|$ ,  $R$  is the “reflection reduction factor,”  $P_p$  is the power which penetrates the wall, and  $P_i$  is the incident one.  $\Gamma$  and the reflected field  $\overline{E}_R$  can be determined using the well-known Fresnel reflection coefficients. Assuming that  $P_p/P_i$  is weekly dependent on the characteristics of wall irregularities as in [11], we can neglect its dependence with  $S$ , that is, the greater  $S$ , the lower  $R$ . With this assumption the power balance for an ideal, smooth wall becomes ( $R = 0$ ,  $R = 1$ )

$$1 = \Gamma^2 + P_p/P_i. \quad (3)$$

Combining (2) and (3), a simple relation between  $R$  and  $S$  can be obtained

$$R \cong \sqrt{1 - \frac{S^2}{\Gamma^2}}. \quad (4)$$

Since  $S$  and  $R$  are real parameters in the range  $[0,1]$  and  $\Gamma$  depends on the incidence direction, if  $S$  is assumed to be a constant, (4) means that  $S$  cannot exceed the minimum among the possible values of  $\Gamma$ .

Following the second approach, the scattering coefficient is defined as:

$$S = \frac{|\overline{E}_S|}{|\overline{E}_R|} \Big|_{ds} \quad (5)$$

According to this definition,  $S^2$  is the percentage of the power which is scattered in all directions at the expenses of the reflected power only. Therefore, the power balance can be rewritten as

$$\begin{aligned} \frac{|\overline{E}_i|^2}{2\eta} ds \cos \theta_i &= R^2 \frac{|\overline{E}_R|^2}{2\eta} ds \cos \theta_i \\ &+ S^2 \frac{|\overline{E}_R|^2}{2\eta} ds \cos \theta_i + P_p \\ &= R^2 \Gamma^2 \frac{|\overline{E}_i|^2}{2\eta} ds \cos \theta_i \\ &+ S^2 \Gamma^2 \frac{|\overline{E}_i|^2}{2\eta} ds \cos \theta_i + P_p \end{aligned}$$

where  $\eta$  is the intrinsic impedance of the medium. Therefore

$$1 = \Gamma^2(R^2 + S^2) + P_p/P_i. \quad (6)$$

Similarly to the previous model, a relation between  $S$  and  $R$  can be obtained

$$R \cong \sqrt{1 - S^2}. \quad (7)$$

Hence, adopting the second approach  $S$  and  $R$  are both independent from the incidence direction and  $S$  can assume any value in the range  $[0,1]$ .

The main difference between the two categories of ER models mentioned above is the definition of the scattering parameter  $S$ , but in both types of models the following synthetic relation (scattering power balance) must be satisfied

$$\begin{aligned} S^2 \cdot U^2 \cdot |\overline{E}_i|^2 \cdot d\Omega_i \cdot r_i^2 &= \int_{2\pi} |\overline{E}_s|^2 d\Omega_s \cdot r_s^2 \\ &= \int_0^{\pi/2} \int_0^{2\pi} |\overline{E}_s|^2 \cdot r_s^2 \cdot \sin \theta_s d\theta_s d\phi_s \quad (8) \end{aligned}$$

where  $d\Omega_i$  is the solid angle of the ray tube impinging on the surface element  $dS$ , and  $r_i, r_s$  are the distances between  $dS$  and source and reception points, respectively (Fig. 1).

$U$  is a function depending on the definition adopted for the  $S$  parameter, and its value is

$$U = \begin{cases} 1 & \text{if } S = |\overline{E}_S|/|\overline{E}_i| \\ \Gamma & \text{if } S = |\overline{E}_S|/|\overline{E}_R|. \end{cases} \quad (9)$$

Introducing the actual assumed shape of the scattered wave  $|\overline{E}_s(r_s, \theta_s, \phi_s)|$  (i.e., the scattering pattern) in (8), its maximum amplitude  $E_{S0}$  can be derived. The shape of the scattering pattern of the wall strongly depends on the characteristics of wall irregularities (windows, balconies, irregular brick, surface roughness, indentations, etc.), so three different kinds of scattering patterns have been considered, each one representative of a practical situation.

*Model 1 (Lambertian Model):*

$$|\overline{E}_s|^2 = E_{S0}^2 \cdot \cos \theta_s. \quad (10)$$

The “scattering radiation lobe” is assumed to have its maximum in the direction perpendicular to the wall; the exact expression of  $E_{S0}$  can be computed from (8), therefore, getting [11], [12]

$$|\overline{E}_s|^2 = \left( \frac{K \cdot S}{r_i \cdot r_s} \right)^2 \cdot U^2 \cdot \frac{\cos \theta_i \cdot \cos \theta_s}{\pi} dS$$

where  $K$  is a constant depending on the amplitude of the impinging wave [12].

*Model 2 (Directive Model):* This model is based on the assumption that the scattering lobe is steered towards the direction

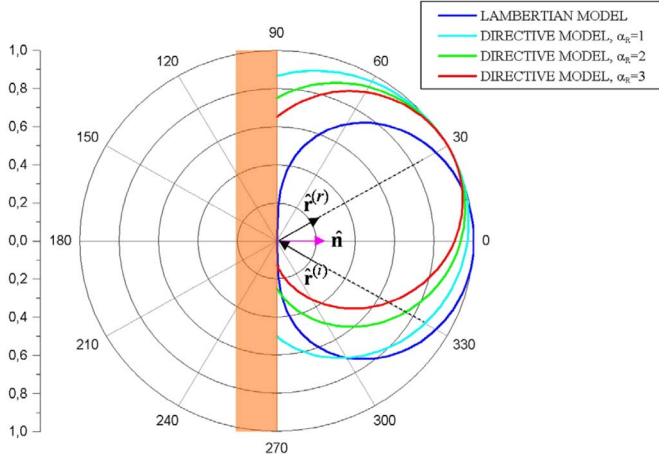


Fig. 2. Comparison of lambertian and single-lobe directive scattering patterns.

of the specular reflection. In order to comply with this assumption, the following expression is considered:

$$|\overline{E}_S|^2 = E_{S0}^2 \cdot \left( \frac{1 + \cos \psi_R}{2} \right)^{\alpha_R} \quad \alpha_R = 1, 2, \dots, N \quad (11)$$

where  $\psi_R$  is the angle between the direction of the reflected wave and the scattering direction  $(\theta_s, \phi_s)$  (Fig. 1), and the exponent  $\alpha_R$  is related to the width of the scattering lobe (i.e., the model directivity). According to (11), it is evident that the maximum is for  $\Psi_R = 0$  (i.e., in the direction of specular reflection); moreover, the greater  $\alpha_R$ , the narrower the scattering lobe. In Fig. 2, the normalized scattering patterns of the directive scattering model (for  $\alpha_R = 1, 2, 3$ ) are shown w.r.t. the Lambertian model, for an incidence angle of  $30^\circ$ .

The maximum amplitude  $E_{S0}$  can be computed by expressing the  $\psi_R$  angle through the incidence and scattering directions, and then solving (8). Through some algebraic manipulations, the following expression has been obtained (see Appendix for details):

$$E_{S0}^2 = \left( \frac{SK}{r_i r_s} \right)^2 U^2 \frac{dS \cos \theta_i}{F_{\alpha_R}}$$

where

$$F_{\alpha_R} = \frac{1}{2^{\alpha_R}} \cdot \sum_{j=0}^{\alpha_R} \binom{\alpha_R}{j} \cdot I_j$$

and

$$I_j = \frac{2\pi}{j+1} \cdot \left[ \cos \theta_i \cdot \sum_{w=0}^{j-1} \binom{j-1}{w} \cdot \frac{\sin^{2w} \theta_i}{2^{2w}} \right] \left( \frac{1 - (-1)^j}{2} \right)$$

**Model 3 (Backscattering Lobe Model):** This model is similar to the directive single-lobe model, but it includes an additional term accounting for backscattering phenomena. In fact, in several practical situations, for example in presence of very protruding surface irregularities (balconies, columns, etc.) and with grazing incidence angles, the diffuse scattering can orig-

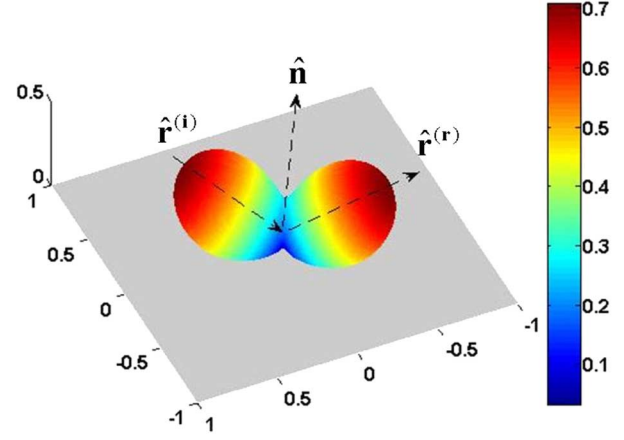


Fig. 3. 3-D pattern of the double-lobe scattering model, for  $\alpha_i = \alpha_R = 10$ ,  $\Lambda = 0.5$ , and  $\theta_i = \pi/4$ .

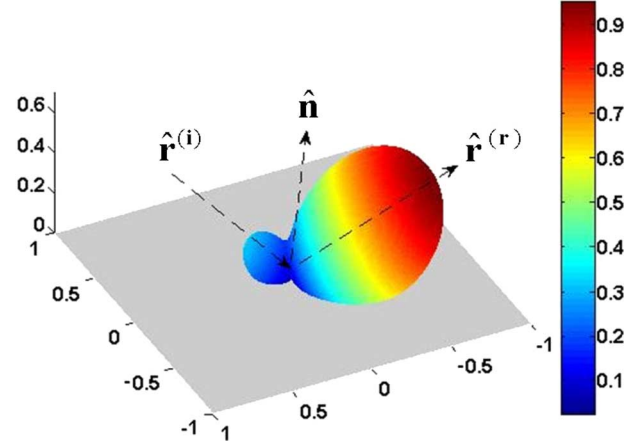


Fig. 4. 3-D pattern of the double-lobe scattering model, for  $\alpha_i = \alpha_R = 10$ ,  $\Lambda = 0.9$ , and  $\theta_i = \pi/4$ .

inate non negligible contributions even in the proximity of the incidence direction (“billiard effect”). A scattering lobe in the incident direction is therefore introduced. The expression of the double-lobe model is

$$|\overline{E}_S|^2 = E_{S0}^2 \cdot \left[ \Lambda \left( \frac{1 + \cos \psi_R}{2} \right)^{\alpha_R} + (1 - \Lambda) \left( \frac{1 + \cos \psi_i}{2} \right)^{\alpha_i} \right] \quad \alpha_i, \alpha_R = 1, 2, \dots, N; \Lambda \in [0, 1] \quad (12)$$

where  $\alpha_i$ , determine the width of the back-lobe and  $\Lambda$  is the repartition factor between the amplitudes of the two lobes.  $\alpha_i$  and  $\alpha_R$  have the same meaning as in the previous model (if  $\alpha_i$  or  $\alpha_R$  increase, the width of the respective lobe decrease).  $\Lambda$  can vary in the range  $[0, 1]$ , and for  $\Lambda = 1$  the model reduces to the single-lobe model seen above. In Figs. 3 and 4, two examples of 3-D double-lobe scattering patterns are shown, for an incidence angle of  $\pi/4$ ,  $\Lambda = 0.5$ , or  $0.9$ , respectively, and for arbitrary values of the other parameters.

The maximum amplitude  $E_{S0}$  of the scattered field for the double-lobe model, can be computed by expressing the angles  $\alpha_i$  and  $\alpha_R$  through the incidence, reflection and scattering directions, and then solving (8). Through some algebraic manipula-

tions, the following expression has been obtained (see Appendix for details):

$$E_{S0}^2 = \left( \frac{SK}{r_i r_s} \right)^2 \cdot U^2 \cdot \frac{dS \cos \theta_i}{F_{\alpha_i, \alpha_R}}$$

where

$$F_{\alpha_i, \alpha_R} = \frac{\Lambda}{2^{\alpha_R}} \cdot \left[ \sum_j \binom{\alpha_R}{j} \cdot I_j \right] + \frac{(1-\Lambda)}{2^{\alpha_i}} \cdot \left[ \sum_j \binom{\alpha_i}{j} \cdot I_j \right]$$

and

$$I_j = \frac{2\pi}{j+1} \cdot \left[ \cos \theta_i \cdot \sum_{w=0}^{\frac{j-1}{2}} \binom{2w}{w} \cdot \frac{\sin^{2w} \theta_i}{2^{2w}} \right] \cdot \left( \frac{1-(-1)^j}{2} \right)$$

All the ER models seen above allow to estimate the amplitude of the scattered field  $\vec{E}_s(r_s, \theta_s, \phi_s)$ , but a complete model should also take into account its polarization characteristics. In general, due to the nature of diffuse scattering phenomena, which are the macroscopic effect of a large number of micro-interactions originated by wall irregularities,  $\vec{E}_s(r_s, \theta_s, \phi_s)$  can be assumed an incoherent, non-polarized wave. Nevertheless, if the observation point  $P_s(r_s, \theta_s, \phi_s)$  is fixed, a local polarization of the vector  $\vec{E}_s$  must still be present. In particular, assuming that the scattered field is polarized on a plane perpendicular to the propagation direction  $\vec{r}_s$ , as should be in the far-field region, and referring to a spherical reference system centred on the wall element (Fig. 1),  $\vec{E}_s$  can be decomposed into two linearly polarized components (along  $\hat{\theta}_s$  and  $\hat{\phi}_s$ ). Furthermore, assuming for the time being that scattering is non-selective toward one or another component, i.e., the two components have equal intensities, the scattered field can be written as

$$\vec{E}_s = \left[ \frac{1}{\sqrt{2}} |\vec{E}_s| e^{j\chi_{\theta s}} \right] \hat{\theta}_s + \left[ \frac{1}{\sqrt{2}} |\vec{E}_s| e^{j\chi_{\phi s}} \right] \hat{\phi}_s \quad (13)$$

where  $|\vec{E}_s|$  can be computed using the proposed scattering models, while the phases  $\chi_{\theta s}$  and  $\chi_{\phi s}$  are *a-priori* unknown, due to the incoherent nature of the ER model. Since the ER models do not account for the phases of the components, the polarization of  $\vec{E}_s$  is also unknown. However, it is still possible to evaluate the scattered power  $P_s$  captured by an Rx antenna (see Section IV). For example, a linearly polarized, dipole antenna would capture half of the power coming from a scattered ray, etc.

### III. THE MEASUREMENT CAMPAIGN

The measurement campaign consists in a set of CW measurements of the power scattered by three different building walls, with the Tx and the Rx equipped with directive antennas oriented toward the center of the wall. Frequency was 1296 MHz, Tx power about 9 dBm, and the total cable losses were of about 5 dB. Three different types of building wall have been considered, each one representative of a different class: a metal, relatively smooth wall of an airport hangar, an uniform brick wall of a warehouse, and a typical brick wall with windows, doors and other elements of a rural building. All walls were nearly

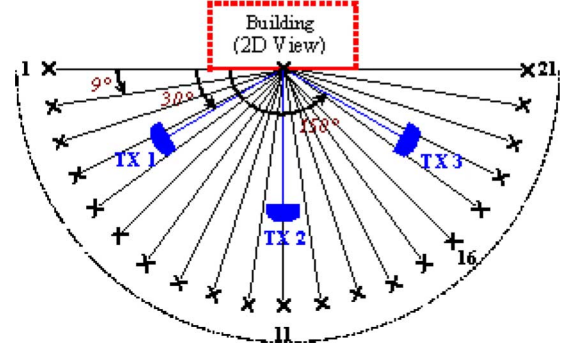


Fig. 5. Tx and Rx positions (top view).

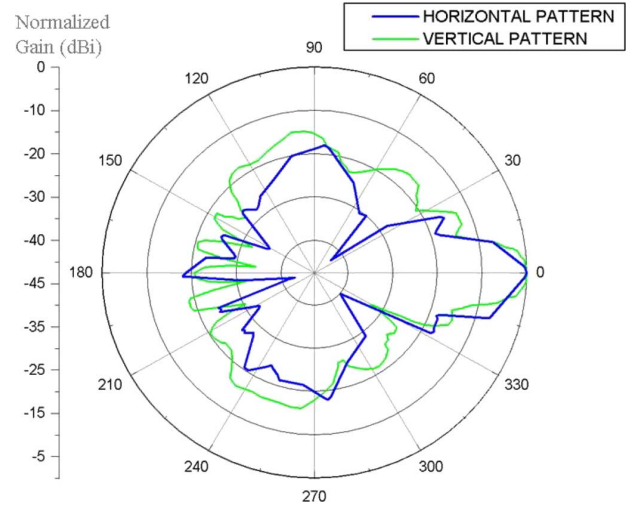


Fig. 6. 1 m parabolic TX antenna: 2-D radiation patterns.

the same height of about 10 by 6 m. A parabolic antenna with 1.5 m diameter was used in the Rx, while two different types of antenna were used to illuminate the wall: a circular horn antenna and a parabolic antenna with 1 m diameter. The wall was illuminated in two different modes: *normal* incidence (Tx2 in Fig. 5) and *slant* incidence (Tx1 and Tx3). It is worth noticing that Tx1 and Tx3 are not equivalent, because the radiation pattern of the antennas is not perfectly symmetric (see Figs. 6–8 in Section VI).

The Rx antenna was moved on equispaced points (angular separation of 9°) on a semicircle centred in the center of the wall. Rx antenna and annexed equipment (cables, receiver, and a spectrum analyzer) were placed on a trolley equipped with an electromechanical pointing system with a video camera.

Finally, in each case, the distance of the antennas from the wall center was determined so that the -6 dB main lobe footprint on the wall would be all contained into the wall frame, in order to minimize the effect of the horizontal top edge and of surrounding objects (which were in all cases quite far). Since the size of the footprint is small with respect to the Rx antenna distance, the wall can be considered “far” as concerns its scattering behavior [13]. The chosen distance was 3.8 m for the horn antenna, 9 m for the 1 m parabolic antenna, and 13 m for the 1.5 m parabolic antenna. Tx and Rx antennas were always at a



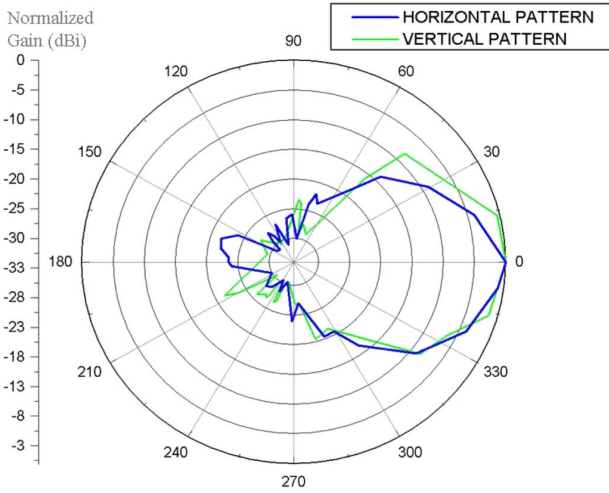


Fig. 7. Horn TX antenna: 2-D radiation patterns.

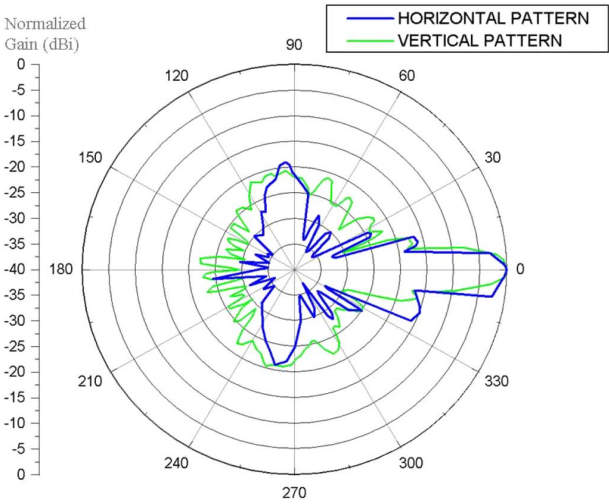


Fig. 8. 1.5 m parabolic TX antenna: 2-D radiation patterns.

height of 3 m from the ground. Given the relatively small distances, the Rx antenna was not in far field w.r.t. the Tx antenna for every Tx/Rx position. However, comparing measurements with RT simulations in reference, free space cases, we observed that deviations due to near-field effect were of the order of only a few decibels.

#### IV. THE RT SIMULATOR

All results reported in the paper are obtained using the 3-D Ray Tracing simulator described in [13]. The performance of this software is improved w.r.t. traditional RT simulators through the introduction of the ER diffuse scattering model. Rays which experienced at least one diffuse scattering interaction along their path are treated incoherently by the program (see below). The field carried by the  $i$ th ray at the Rx point can be summarized with the following synthetic formula [13]:

$$\vec{E}_i(\text{Rx}) = \left\{ \prod_{j=0}^{N_{EV}^i} [\vec{D}^{o(i,j)}(P_{i,j})] \vec{E}_{i0}(\text{Tx}) \right\} \cdot A(o(i,j), s_j, j=0, \dots, N_{EV}^i) \quad i=1, \dots, N_r \quad (14)$$

where  $N_r$  is the number of rays,  $N_{EV}^i$  is the number of the interactions experienced by the  $i$ th ray,  $\vec{E}_{i0}(\text{Tx})$  is the field at a reference distance of 1 m from the Tx (in the direction of the  $i$ th ray),  $o(i,j)$  represents the kind of interaction (reflection, diffraction, scattering),  $P_{i,j}$  represents the spatial point where the  $j$ th interaction is assumed to take place,  $\vec{D}$  is an appropriate dyadic to decompose the field into orthogonal components at the point  $P_{i,j}$  and includes the proper attenuation coefficients (reflection coefficients, diffraction coefficients, etc.). Finally,  $A$  represents the overall divergence factor which depends on the lengths  $s_j$  ( $j=0, \dots, N_{EV}^i$ ) of the segments composing the  $i$ th path and on the interactions experienced by the ray. For each ray, the contribution to the received power is computed combining the field expressed in (14) with the gain and the polarization of the Rx antenna in the direction of the incoming ray, then all coherent contributions are summed taking into account modules and phases, getting the total coherent power  $P_c$  at the Rx.

Each ray undergoing at least one diffuse scattering interaction is assumed “incoherent.” The field at the Rx is still computed through an “incoherent version” of formula (14) since formulas (10)–(12) can all be easily expressed as products of the transmitted field module  $|\vec{E}_{i0}(\text{Tx})|$  multiplied by a “scattering coefficient.” The power, however, is repartitioned in equal parts along the two components on the wavefront each time a scattering occurs according to (13), and in addition any phase information is disregarded from there forth. The overall incoherent power  $P_{\text{scat}}$  is computed summing incoherently all the power contributions of incoherent rays.

Finally, the incoherent rays power  $P_{\text{scat}}$  is summed to the coherent rays power  $P_c$  therefore obtaining the total received power

$$P_{\text{tot}}(\text{Rx}) = P_c + P_{\text{scat}}. \quad (15)$$

#### V. THE VALIDATION METHOD

The models proposed in Section II are checked with measurements according to the following procedure. Since it is impossible to single out only the diffuse scattering contribution from measurements, due to the limited directivity of the available antennas, measurements have been compared with accurate 3-D RT simulations for all the considered wall topologies. Such RT simulations include specular reflection and UTD edge diffraction and consider the detailed radiation patterns of the antennas (see Figs. 6–8). Standard electromagnetic characteristics were used for brick walls [ $\epsilon_r = 5$ ,  $\sigma = 1.e - 2$  (conductivity)] and of course perfect conductor characteristics for the metal hangar wall. The adopted 3-D RT program [13] was equipped with all of the scattering models described in Section II.

For simplicity, and due to the relatively small dimension of the illuminated footprint on the wall with respect to the Rx distance, a single scattered ray is computed for each Rx which is assumed to spring from the center of the wall, similarly to what is assumed in [13] for “far walls.” The tuning of the scattering model is quite accurate because the scattering contribution is almost always dominant, except in the specular reflection and in back-to front peaks (see Figs. 10–16 in Section VI).

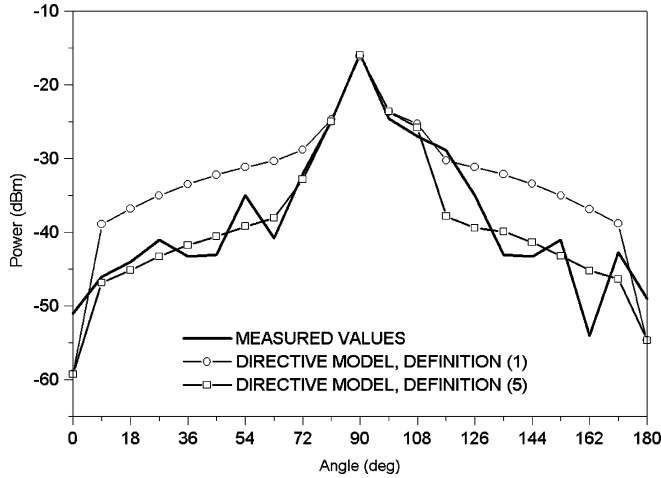


Fig. 9. Comparison of models using different definitions of the scattering coefficient—Brick wall; Tx antenna at  $90^\circ$ .

## VI. RESULTS

Comparisons between measurements and RT predictions are shown in this section. All figures show the received power (measured and simulated) versus the Rx angular position. All the antennas used in the measurement campaign have been preliminarily characterized on both the horizontal and the vertical plane. In Fig. 6 and 7 the 2-D radiation patterns of the Tx antennas (1 m parabolic and horn), are reported.

In Fig. 8 the 2-D radiation patterns of the Rx antenna (1.5 m parabolic) are reported.

In all cases, except where otherwise stated, the 1 m parabolic antenna is used at the Tx and the 1.5 m parabolic antenna is used at the Rx. Regarding polarization, results with both antennas having vertical excitations are shown, but further considerations on results with antennas in cross-polarized configurations are reported at the end of the section. Preliminarily, comparisons between measurements and RT simulations have been carried out in order to determine which definition of the scattering coefficient, between the (1) and the (5), better fits measurements. It has been found that adopting the first definition, it is difficult to find a single value of  $S$  valid for both slant and normal illumination of the wall. On the contrary, adopting definition (5), it is possible to obtain good results for both normal and slant illumination, keeping  $S$  constant.

In Fig. 9 it is shown that assuming the optimum  $S$  value for slant illumination ( $S = 0.2$ , for the brick wall), a good agreement with measurements can be obtained also for normal illumination if definition (5) is adopted, whereas received power is overestimated adopting definition (1). Therefore, all results shown in the following are related to definition (5).

Regarding the shape of the scattering pattern, further investigations have been performed in order to find the best ER model at minimum squares (minimum RMS distance). The single-lobe model demonstrated to be the best for all types of considered wall. Therefore the backscattering phenomena are not very important in the considered scenarios, probably due to the absence of very protruding irregularities.

In Figs. 10 and 11, a comparison obtained with the single-lobe model (model 2) for different values of the parameter  $\alpha_R$  is

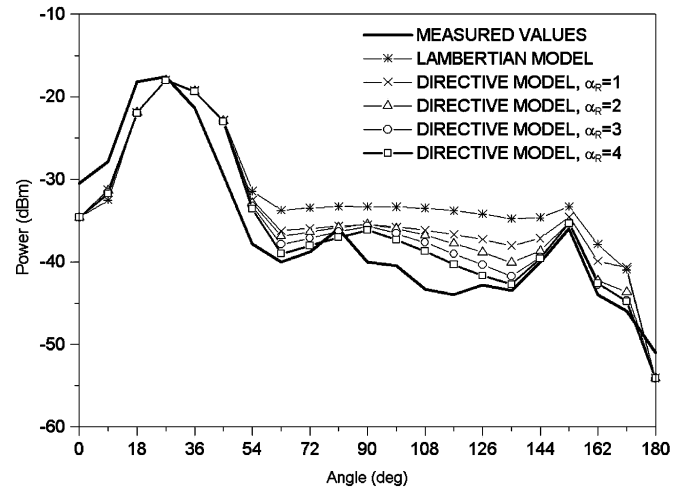


Fig. 10. Comparison of models—Brick wall; Tx antenna at  $150^\circ$ .

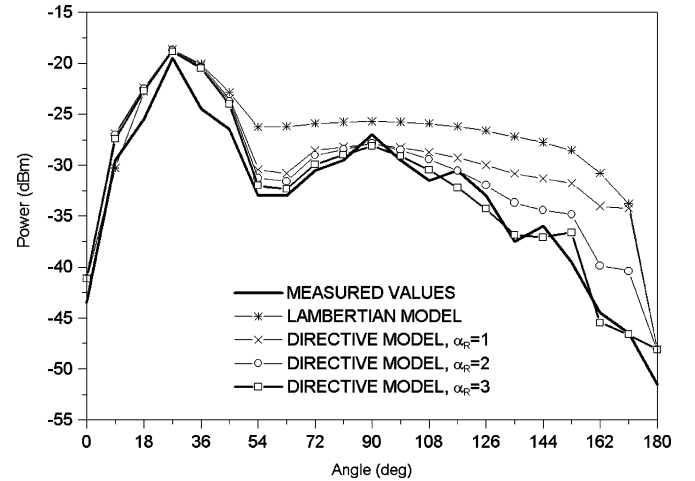


Fig. 11. Comparison of models—Rural building; Tx antenna at  $150^\circ$ .

TABLE I  
RMS DISTANCE BETWEEN SIMULATED AND MEASURED CURVES  
REPORTED IN FIG. 11

Scattering Model	RMS distance from measured values (dBm)
Lambertian Model	6.67
Model 2, $\alpha_R=1$	4.81
Model 2, $\alpha_R=2$	2.85
Model 2, $\alpha_R=3$	1.85

shown, in the case of the wall illuminated by a Tx antenna (1 m parabolic) pointed at  $150^\circ$  with respect to the wall plane (position 3 in Fig. 5). The former shows the results obtained for the brick wall, the latter shows the same result for the rural building wall. The scattering coefficient  $S$  was set to 0.2 for the brick wall, and to 0.4 for the rural building wall. In both figures also the results obtained using the Lambertian model (model 1) are reported, as a reference case. From the comparison it is evident that using the directive model the agreement is good in the central part of the graph whereas using the Lambertian model in the same zone the scattered power appears overestimated.

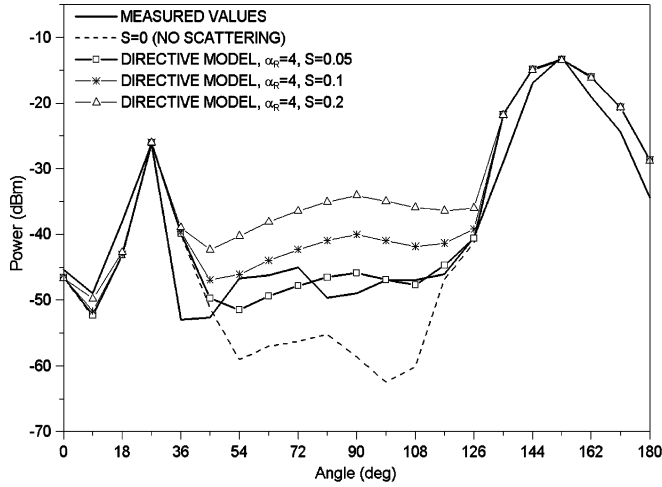


Fig. 12. Hangar wall illuminated with 1 m parabolic antenna at 30°.

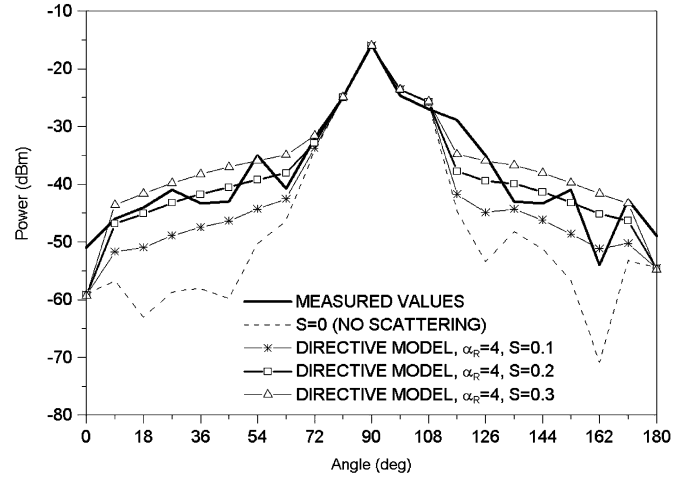


Fig. 15. Brick wall; Tx antenna at 90°.

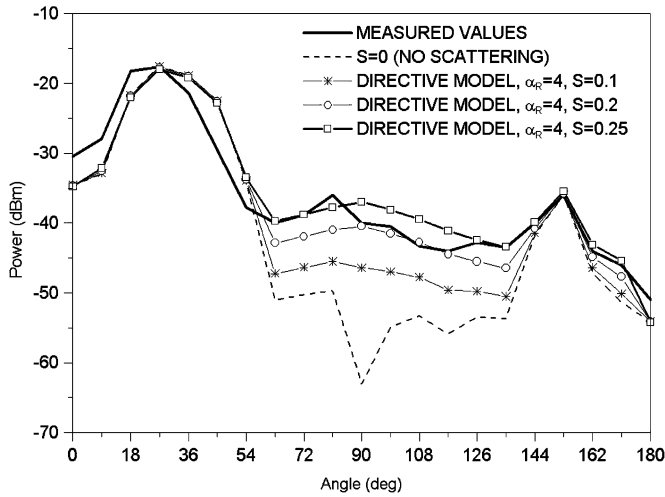


Fig. 13. Brick wall; Tx antenna at 150°.

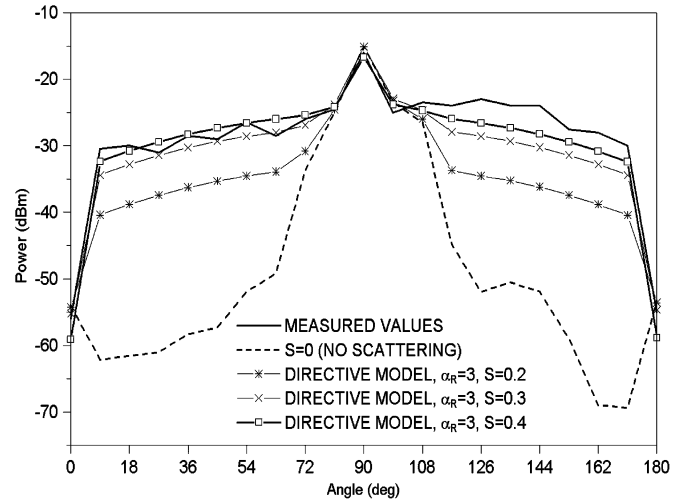


Fig. 16. Rural building; Tx antenna at 90°.

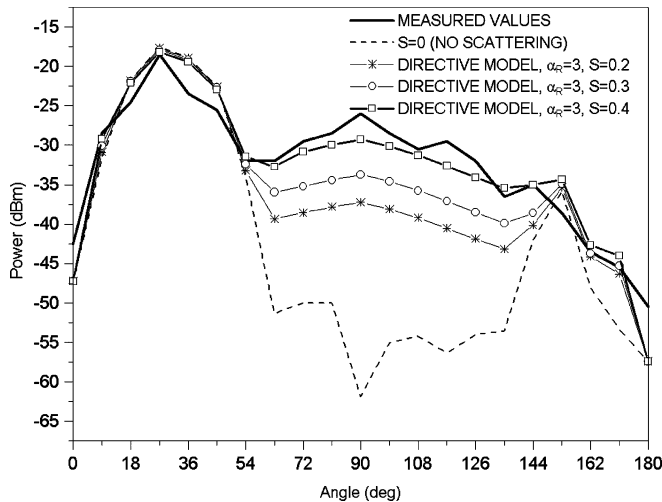


Fig. 14. Rural building; Tx antenna at 150°.

For the brick wall,  $\alpha_R = 4$  has been found to be the value that guarantees the best RMS agreement with the measurements (Fig. 10), while  $\alpha_R = 3$  gives the best fit for the rural building

wall (Fig. 11). This is not evident from Fig. 11 since the different curves are partially overlapped. However the respective RMS distances are reported in Table I, and  $\alpha_R = 3$  is proved to give the best fit.

$\alpha_R = 4$  has been found to be the best-fit value also for the hangar wall. The lower value of the  $\alpha_R$  parameter found for the rural building is probably due to the large number of irregularities typical of this wall, which reduce the directivity of the scattering pattern.

In Figs. 12–16 comparisons between measurements and predictions for different values of the  $S$  parameter are shown: in all cases the single lobe ER model is adopted, which demonstrated to be the best in all topologies. All predictions are obtained using the directive model as a function of different  $\alpha_R$  and  $S$  values, adopting the best RMS value for the fixed parameter ( $\alpha_R$ ), determined according to the procedure explained above, and varying  $S$ . In all the graphs, the dashed line represents prediction without scattering ( $S = 0$ ).

Fig. 12 shows the received power versus Rx position as a function of  $S$  for the hangar wall case. The predicted power without scattering is slightly underestimated at some points, whereas using  $S = 0.05$  a good agreement with measurements

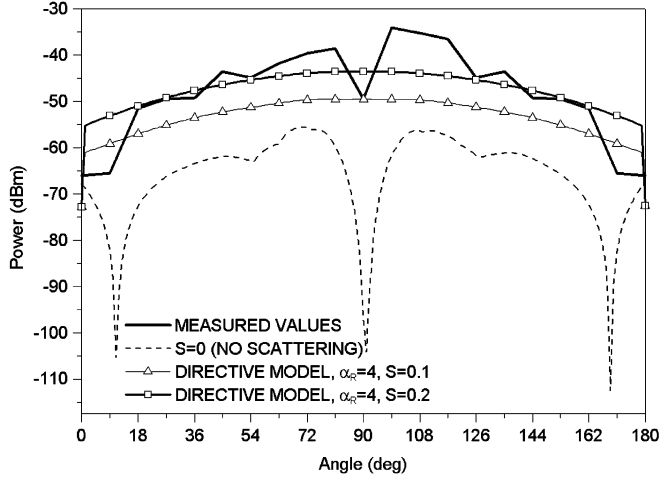


Fig. 17. Brick wall illuminated with the horn antenna at 90°: Tx and Rx antennas in cross-polarized configuration.

is achieved everywhere. Therefore, in this case the scattering is useful for getting a good prediction in all receiving positions, but results obtained using traditional RT simulators (which do not take into account diffuse scattering) are still acceptable.

Similar results are shown in Fig. 13 for the brick wall. In this case the best value of  $S$  is of about 0.2. Moreover, the figure shows that neglecting the contribution of scattering (i.e., assuming  $S = 0$ ), the received power is underestimated in some central positions by as much as 20 dB.

Finally, Fig. 14 shows that predictions with  $S = 0$  are totally incorrect for a rural building wall, which is quite representative of many classes of real building walls: therefore in such cases the introduction of diffuse scattering is definitely necessary to get good results. The best value for  $S$  is 0.4 in this case, in agreement with previous studies [11]–[13].

In Figs. 15 and 16, the results for the brick wall and the rural building wall are shown in the case of normal illumination. Again, the results show the importance of diffuse scattering on propagation, and the optimum  $S$  values are the same as for slant illumination.

In Fig. 17, the results for the brick wall with normal incidence and with antennas in cross-polarized configuration are shown. In particular, results are obtained using the horn antenna with vertical excitation at the Tx, and the 1.5 m parabolic antenna with horizontal excitation at the Rx. Comparing measurement and simulation it can be noticed that, again, proper modeling of scattering is necessary to get correct received power values. A good agreement is obtained using the single-lobe model with the same parameter values which have been found to be optimum for the brick wall with antennas in co-polar configurations ( $\alpha_R = 4$ ,  $S = 0.2$ ). The non-idealities of antennas (which can perturb the polarization of the field, increasing the coupling between antennas) have not been modeled so far. On the other hand, these non-idealities probably affect measured values (due, for example, to diffraction on the border of parabolic plate). For this reason, through simulations it is not possible to reproduce all received power fluctuations, however adding scattering the average behavior is fairly predicted.

## VII. CONCLUSION

A measurement campaign aimed at determining the scattering pattern of typical building walls is described in the paper. In addition, the ER diffuse scattering model [11], [12] is modified and tuned to get the best agreement with measurements. Different shapes of the scattering pattern are hypothesized, and for each of them a simple, parametric expression is provided, which can be easily implemented and embedded into RT simulators. It is shown that the “single-lobe directive model” (with the lobe steered toward the specular direction) is the best in all cases, assuming  $\alpha_R = 4$  for the hangar and the brick wall, and  $\alpha_R = 3$  for the rural building wall. Besides, the optimum scattering coefficient  $S$  values are of 0.05, 0.2, and 0.4 in the three considered topologies, respectively. Being the latter topology quite representative of simple, brick-wall suburban buildings, we can infer that  $S = 0.4$  is a realistic value for field prediction in suburban areas, in agreement with previous work [11]–[13]. In the future, further investigations must be done in order to evaluate the best scattering model for urban buildings with protruding masonry (columns, indentations, etc.) which probably originate a more significant backscattering effect even far from the specular direction. Besides, simulations in dense urban environment would probably require even greater values of  $S$ , i.e., a greater diffuse scattering contribution.

## APPENDIX

In this Appendix, the mathematical procedure to derive the complete expressions of the proposed scattering patterns is provided. First, the procedure for the single lobe directive model is explained, and then the method is extended to the double lobe model.

### A. Directive Model

Preliminarily it is helpful to express the angle  $\Psi_R$  between scattering and specular reflection directions through the incidence and scattering directions adopting a reference system centred on the wall element. Referring to a Cartesian reference system having the  $z$ -axis on the normal to the element, and to a spherical reference system centred on the wall element too (see Fig. 1), the reflection and scattering directions  $\hat{\mathbf{r}}^{(r)}$ ,  $\hat{\mathbf{r}}^{(s)}$  can be easily expressed as

$$\begin{aligned}\hat{\mathbf{r}}^{(r)} &= -\sin\theta_i \cos\varphi_i \cdot \hat{\mathbf{i}} - \sin\theta_i \sin\varphi_i \cdot \hat{\mathbf{j}} + \cos\theta_i \cdot \hat{\mathbf{k}} \\ \hat{\mathbf{r}}^{(s)} &= \sin\theta_s \cos\varphi_s \cdot \hat{\mathbf{i}} + \sin\theta_s \sin\varphi_s \cdot \hat{\mathbf{j}} + \cos\theta_s \cdot \hat{\mathbf{k}}.\end{aligned}$$

Furthermore, with the chosen reference systems, the elevations  $\theta_i$  and  $\theta_s$  correspond to the incidence and scattering angles w.r.t. the normal to the wall element.

By means of simple trigonometric manipulations, it can be shown that

$$\begin{aligned}\cos\psi_R &= \hat{\mathbf{r}}^{(r)} \cdot \hat{\mathbf{r}}^{(s)} \\ &= -\sin\theta_i \sin\theta_s \cdot \cos(\varphi_s - \varphi_i) + \cos\theta_i \cos\theta_s.\end{aligned}\quad (\text{A1})$$

Remembering that  $|\bar{E}_i| = K/r_i$ , where  $K$  is a constant depending on the amplitude of the impinging wave [12], and observing that  $d\Omega_i = dS \cos\theta_i/r_i^2$ , the maximum amplitude of



the scattered wave at the reception point can be obtained by applying (8)

$$E_{S0}^2 = \left( \frac{SK}{r_i r_s} \right)^2 U^2 \frac{dS \cos \theta_i}{F_{\alpha_R}}. \quad (A2)$$

where

$$\begin{aligned} F_{\alpha_R} &= \int_0^{\frac{\pi}{2}} \int_0^{2\pi} \left( \frac{1 + \cos \psi_R}{2} \right)^{\alpha_R} \sin \theta_s d\theta_s d\varphi_s \\ &= \frac{1}{2^{\alpha_R}} \int_0^{\frac{\pi}{2}} \int_0^{2\pi} (1 + \cos \psi_R)^{\alpha_R} \sin \theta_s d\theta_s d\varphi_s. \end{aligned}$$

Given the general expression of the scattered field which includes the term  $F_{\alpha_R}$  seen above, the aim of what follows is now to solve the integral in (A2) and to find an analytical formulation of it through the parameter  $\alpha_R$ . By using the Newton's binomial formula,  $F_{\alpha_R}$  can be expressed as

$$F_{\alpha_R} = \frac{1}{2^{\alpha_R}} \cdot \sum_{j=0}^{\alpha_R} \binom{\alpha_R}{j} \cdot I_j \quad (A3)$$

where

$$I_j = \int_0^{\frac{\pi}{2}} \int_0^{2\pi} (\cos \psi_r)^j \sin \theta_s d\theta_s d\varphi_s.$$

Thus, the study of the term  $F_{\alpha_R}$  is now reduced to the evaluation of the terms of the power series in (A3). Through the relation (A1), it is easy to evaluate these terms. Studying their dependence with  $\alpha_R$  it can be shown that the even terms do not depend on the incidence direction, and, in particular

$$I_{j(\text{even})} = \frac{2\pi}{j+1}.$$

In a similar way, it can be shown that the odd terms depend only on the angle  $\theta_i$  (i.e., on the incidence angle), and they vary following the formula:

$$I_{j(\text{odd})} = \frac{2\pi}{j+1} \cos \theta_i \cdot K_n \quad n = \frac{j-1}{2}$$

where  $K_n$  is the sum of the first  $n$  elements of the series

$$\sum_w \binom{2w}{w} \cdot \frac{\sin^{2w} \theta_i}{2^{2w}} \quad w = 0, 1, 2, \dots, n, \dots$$

The general formulation for the odd terms of the Newton's formula is then

$$I_{j(\text{odd})} = \frac{2\pi}{j+1} \cdot \left\{ \cos \theta_i \cdot \sum_{w=0}^{(j-1)/2} \binom{2w}{w} \cdot \frac{\sin^{2w} \theta_i}{2^{2w}} \right\}.$$

Since both even and odd terms include the factor  $2\pi/(j+1)$ , it is possible to unify their expressions in a more general formula, by introducing an exponent that cancels the additional contribution depending on  $\theta_i$  for all the even terms

$$I_j = \frac{2\pi}{j+1} \cdot \left\{ \cos \theta_i \cdot \sum_{w=0}^{(j-1)/2} \binom{2w}{w} \cdot \frac{\sin^{2w} \theta_i}{2^{2w}} \right\}^{\left( \frac{1-(-1)^j}{2} \right)}. \quad (A4)$$

Summing up, the general expression of the scattered wave, valid for any value of the exponent  $\alpha_R$ , can be written as

$$|\overline{E}_s|^2 = \left\{ \left( \frac{SK}{r_i r_s} \right)^2 \cdot U^2 \cdot \frac{dS \cos \theta_i}{F_{\alpha_R}} \right\} \cdot \left( \frac{1 + \cos \psi_R}{2} \right)^{\alpha_R} \quad (A5)$$

with

$$F_{\alpha_R} = \frac{1}{2^{\alpha_R}} \sum_{j=0}^{\alpha_R} \left[ \frac{2\pi}{j+1} \cdot \left\{ \cos \theta_i \cdot \sum_{w=0}^{(j-1)/2} \binom{2w}{w} \cdot \frac{\sin^{2w} \theta_i}{2^{2w}} \right\}^{\left( \frac{1-(-1)^j}{2} \right)} \right].$$

## B. Double-Lobe Model

The procedure to obtain the complete expression of the scattered field is quite similar to the one for the single-lobe model, but two additional parameters must be considered: the exponent  $\alpha_i$  related to the width of the backscattering lobe, and the "repartition factor" of power between the lobes,  $\Lambda$ . Moreover, it is necessary to express the angle  $\psi_i$  between the scattering and incidence directions in function of the spherical coordinates of them, as done in the single-lobe model for the angle  $\psi_R$ . The incidence direction can be expressed by

$$\hat{\mathbf{r}}^{(i)} = \sin \theta_i \cos \varphi_i \cdot \hat{\mathbf{i}} + \sin \theta_i \sin \varphi_i \cdot \hat{\mathbf{j}} + \cos \theta_i \cdot \hat{\mathbf{k}}$$

while the expression of the scattering direction  $\hat{\mathbf{r}}^{(s)}$  can be found in the subparagraph a) of the appendix. By means of simple calculations, it can be shown that

$$\begin{aligned} \cos \psi_i &= \hat{\mathbf{r}}^{(i)} \cdot \hat{\mathbf{r}}^{(s)} \\ &= \sin \vartheta_i \sin \theta_s \cdot \cos(\varphi_s - \varphi_i) + \cos \theta_i \cos \theta_s. \end{aligned} \quad (B1)$$

Applying the power balance to the actual model, similarly to what explained in subparagraph a) for the single-lobe model, the following expression can be obtained:

$$\begin{aligned} |\overline{E}_s|^2 &= \left\{ \left( \frac{SK}{r_i r_s} \right)^2 \cdot U^2 \cdot \frac{dS \cos \theta_i}{F_{\alpha_i, \alpha_R}} \right\} \\ &\cdot \left[ \Lambda \left( \frac{1 + \cos \psi_R}{2} \right)^{\alpha_R} + (1 - \Lambda) \left( \frac{1 + \cos \psi_i}{2} \right)^{\alpha_i} \right] \end{aligned} \quad (B2)$$

where

$$F_{\alpha_i, \alpha_R} = \Lambda F_{\alpha_i} + (1 - \Lambda) F_{\alpha_R}$$

and

$$\begin{cases} F_{\alpha_R} = \frac{1}{2^{\alpha_R}} \cdot \sum_{j=0}^{\alpha_R} \binom{\alpha_R}{j} \cdot I_j^{\alpha_R} \\ F_{\alpha_i} = \frac{1}{2^{\alpha_i}} \cdot \sum_{j=0}^{\alpha_i} \binom{\alpha_i}{j} \cdot I_j^{\alpha_i} \end{cases}$$

$$I_j^{\alpha_R} = \int_0^{\pi/2} \int_0^{2\pi} (\cos \psi_R)^j \sin \theta_s d\theta_s d\varphi_s$$

$$I_j^{\alpha_i} = \int_0^{\pi/2} \int_0^{2\pi} (\cos \psi_i)^j \sin \theta_s d\theta_s d\varphi_s.$$

The term  $I_j^{\alpha_R}$  has the same expression as in subsection A) of this Appendix, while  $I_j^{\alpha_i}$  is slightly different because the angle  $\psi_i$  instead of  $\psi_R$  appears in the integral. Substituting expressions (A1) and (B1) in the integrals above, it is easy to show that some terms in  $(\cos \psi_R)^j$  and  $(\cos \psi_i)^j$  have different signs, but these opposite terms do not contribute to both integrals, so  $I_j^{\alpha_R}$  and  $I_j^{\alpha_i}$  are equal. Therefore, the complete expression of the factor  $F_{\alpha_i, \alpha_R}$  can be written as

$$F_{\alpha_i, \alpha_R} = \frac{\Lambda}{2^{\alpha_R}} \sum_{j=0}^{\alpha_R} \binom{\alpha_R}{j} I_j + \frac{(1-\Lambda)}{2^{\alpha_i}} \sum_{j=0}^{\alpha_i} \binom{\alpha_i}{j} I_j \quad (\text{B3})$$

where  $I_j$  is expressed by (A4). Finally, substituting the expression above in (B2), the general formula for the double-lobe-model scattered field can be obtained.

#### ACKNOWLEDGMENT

The authors would like to thank the Centro Radioastronomico Bagnara di Romagna association and E.S.SAT, Bagnara di Romagna, Italy, for the useful suggestions and for the support in performing the measurements reported in the paper.

#### REFERENCES

- [1] T. Kürner, D. J. Cichon, and W. Wiesbeck, "Concepts and results for 3-D digital terrain-based wave propagation models: an overview," *IEEE J. Select. Areas in Commun.*, vol. 11, no. 7, pp. 1002–1012, Sep. 1993.
- [2] M. C. Lawton and J. P. McGeehan, "The application of a deterministic ray launching algorithm for the prediction of radio channel characteristics in small-cell environments," *IEEE Trans. Veh. Technol.*, vol. 43, pp. 955–969, Nov. 1994.
- [3] G. Liang and H. L. Bertoni, "A new approach to 3-D ray tracing for propagation prediction in cities," *IEEE Trans. Antennas Propag.*, vol. 46, no. 6, pp. 853–863, Jun. 1998.
- [4] H.-J. Li, C.-C. Chen, T.-Y. Liu, and H.-C. Lin, "Applicability of ray-tracing technique for the prediction of outdoor channel characteristics," *IEEE Trans. Veh. Technol.*, vol. 49, no. 6, pp. 2336–2349, Nov. 2000.
- [5] K. Kalliola, H. Laitinen, P. Vainikainen, M. Toeltsch, J. Laurila, and E. Bonek, "3-D double-directional radio channel characterization for urban macrocellular applications," *IEEE Trans. Antennas Propag.*, vol. 51, no. 11, pp. 3122–3133, Nov. 2003.
- [6] J. Laurila, K. Kalliola, M. Toeltsch, K. Hugl, P. Vainikainen, and E. Bonek, "Wideband 3-D characterization of mobile radio channels in urban environment," *IEEE Trans. Antennas Propag.*, vol. 50, no. 2, pp. 233–243, Feb. 2002.
- [7] H. Budiarto, K. Horiata, K. Haneda, and J. Takada, "Experimental study of non-specular wave scattering from building surface roughness for mobile propagation modelling," *IEICE Trans. Commun.*, vol. E87-B, no. 4, pp. 958–966, Apr. 2004.
- [8] M. O. Al-Nuaimi and M. S. Ding, "Prediction models and measurements of microwave signals scattered from buildings," *IEEE Trans. Antennas Propag.*, vol. 42, no. 8, pp. 1126–1137, Aug. 1994.
- [9] C. Kloch and J. Bach Andersen, "Radiosity—an approach to determine the effect of rough surface scattering in mobile scenarios," in *Proc. IEEE AP-S Int. Symp.*, Montreal, Jul. 1997, pp. 890–893.
- [10] D. Didascalou, M. Dottling, N. Geng, and W. Wiesbeck, "An approach to include stochastic rough surface scattering into deterministic ray-optical wave propagation modeling," *IEEE Trans. Antennas Propag.*, vol. 51, no. 7, pp. 1508–1515, Jul. 2003.
- [11] V. Degli-Esposti and H. L. Bertoni, "Evaluation of the role of diffuse scattering in urban microcellular propagation," presented at the IEEE-VTC'99—Fall, Amsterdam, The Netherlands, Sep. 19–22, 1999.
- [12] V. Degli-Esposti, "A diffuse scattering model for urban propagation prediction," *IEEE Trans. Antennas Propag.*, vol. 49, no. 7, pp. 1111–1113, Jul. 2001.
- [13] V. Degli-Esposti, D. Guiducci, A. de'Marsi, P. Azzi, and F. Fuschini, "An advanced field prediction model including diffuse scattering," *IEEE Trans. Antennas Propag.*, vol. 52, no. 7, pp. 1717–1728, Jul. 2004.



**Vittorio Degli-Esposti** (M'94) received the Laurea degree (with honours) and the Ph.D. degree in electronic engineering from the University of Bologna, Italy, in 1989 and 1994, respectively.

From 1989 to 1990, he was with Siemens Telecomunicazioni, Milan, Italy, in the Microwave Communication Group. Since November 1994, he has been with the Dipartimento di Elettronica, Informatica e Sistemistica (DEIS), University of Bologna, where he is now an Associate Professor and teaches courses on radio propagation and antennas.

In 1998, he was a Visiting Researcher at the Polytechnic University, Brooklyn, NY, working with Professor H. L. Bertoni, and, in 2006, he was a Visiting Professor at the Helsinki University of Technology (TKK) where he gave a course on "Urban propagation modelling and ray tracing." He participated in the European Cooperation Projects COST 231–273 and in the European Network of Excellence NEWCOM. He was appointed Editor of Section 4.3 "Deterministic propagation modelling" of the Final Report book of COST 273. He is the author or coauthor of more than 60 technical papers in the fields of applied electromagnetics, radio propagation and wireless systems. His current research interests are in the fields of applied electromagnetics, ultrawideband radio propagation, mobile radio propagation, diffuse scattering models, ray tracing, and advanced models for urban field prediction.

Dr. Degli-Esposti is member of the IEEE Antennas and Propagation Society. He also serves as reviewer for a number of international journals including several IEEE TRANSACTIONS.



**Franco Fuschini** was born in Bologna, Italy, in 1973. He received the Laurea degree (*magna cum laude*) in telecommunication engineering and the Ph.D. degree in electronics and computer science from the University of Bologna, in March 1999 and July 2003, respectively.

He participated in the European Cooperation Project COST 273 and in the European Network of Excellence NEWCOM. He is now a Research Associate at the University of Bologna. His research interests are in the field of mobile communications and particularly of statistical field prediction models and advanced ray tracing simulators for urban propagation, wireless systems and RF-ID systems.



**Enrico M. Vitucci** (S'04) was born in Rimini, Italy, in 1977. He received the Laurea degree in telecommunication engineering from the University of Bologna, Bologna, Italy, in March 2003.

During 2003, he was a collaborator in the Department of Electronics and Information Systems (DEIS), University of Bologna, where he was involved in a research program on digital terrestrial television. In 2004, he started the Ph.D. program in electrical engineering and computer science at the DEIS-University of Bologna. He participated in

the European Cooperation Project COST 273 and in the European Network of Excellence NEWCOM. His current research interests are in mobile radio propagation, ray tracing models, diffuse scattering models, and MIMO channel modelling.

Mr. Vitucci serves as Reviewer for a number of international journals including the IEEE TRANSACTIONS ON ANTENNAS AND PROPAGATION, IEEE TRANSACTIONS ON VEHICULAR TECHNOLOGY, and the IEEE TRANSACTIONS ON WIRELESS COMMUNICATIONS.



**Gabriele Falciasacca** was born in Bologna, Italy, in 1945. He received the Laurea degree in electronic engineering from the University of Bologna.

In 1970, he joined the laboratories of the Fondazione Ugo Bordoni, Pontecchio Marconi, where he was involved in the Italian research program on millimeter waveguide communication systems. Since 1973, he has been with the Institute of Electronics, University of Bologna (now Department of Electronics and Computer Science, DEIS), as an Assistant Professor and a Lecturer on microwave techniques. Since 1980, he has been a Full Professor. From 1994 to 2000, he was appointed Director of the Department of Electronics and Computer Science at the University of Bologna. In February 2001, he was appointed President of the Science, Technology and Enterprise Consortium for Research and Innovation of the Italian Region Emilia-Romagna (ASTER). He has been Chairman of the Guglielmo Marconi Foundation since 1997. He is also a Consultant for the Ugo Bordoni Foundation and Chairman of the Scientific Committee of the Consortium "Elettra2000," devoted to the study and to the diffusion of scientific results in the field of health issues related to electromagnetic waves. He is the author of more than 150 technical papers. His main fields of research are applied electromagnetics, mobile radio and wireless systems, radio propagation models, remote sensing and positioning techniques.